Dissociation of Vibrational State-Selected O 2 + Ions in the B 2 Σ g ⁻ State Using Threshold Photoelectron-Photoion Coincidence Velocity Imaging

5 AUTHORS, INCLUDING:

Xiaofeng Tang
Hefei Institute of Physical Sciences, Chinese …
27 PUBLICATIONS   112 CITATIONS

Xiaoguo Zhou
University of Science and Technology of China
51 PUBLICATIONS   316 CITATIONS

M. L. Niu
VU University Amsterdam
20 PUBLICATIONS   124 CITATIONS

Shilin Liu
University of Science and Technology of China
103 PUBLICATIONS   694 CITATIONS

Dissociation of Vibrational State-Selected O_2^+ Ions in the $B^2\Sigma_g^-$ State Using Threshold Photoelectron−Photoion Coincidence Velocity Imaging

Xiaofeng Tang,[†] Xiaoguo Zhou,*[,†] Mingli Niu,[†] Shilin Liu,[†] and Liusi Sheng[‡]

[†]Hefei National Laboratory for Physical Sciences at the Microscale, Department of Chemical Physics, University of Science and Technology of China, Hefei, Anhui 230026, China

[‡]National Synchrotron Radiation Laboratory, University of Science and Technology of China, Hefei, Anhui 230029, China

ABSTRACT: Using the recently developed threshold photoelectron−photoion coincidence (TPEPICO) velocity imaging mass spectrometer (Tang et al. *Rev. Sci. Instrum.* **2009**, *80*, 113101), dissociation of vibrational state-selected $O_2^+(B^2\Sigma_g^-$ $v^+ = 0{-}6)$ ions was investigated. Both the speed and angular distributions of the O^+ fragments dissociated from individually vibronic levels of the $B^2\Sigma_g^-$ state were obtained directly from the three-dimensional time-sliced TPEPICO velocity images. Two dissociation channels, $O^+(^4S) + O(^3P)$ and $O^+(^4S) + O(^1D)$, were respectively observed, and their branching ratios were found to be heavily dependent on the vibrational states. A new intersection mechanism was suggested for the predissociation of $O_2^+(B^2\Sigma_g^-)$ ions, especially for dissociation at the energy of the $v^+ = 4$ level. In addition, the anisotropic parameters for O^+ fragments from different dissociative pathways were determined to be close to zero, indicating that the $v^+ = 0{-}6$ levels of $B^2\Sigma_g^-$ predissociate on a time scale that is much slower than that of molecular rotation.
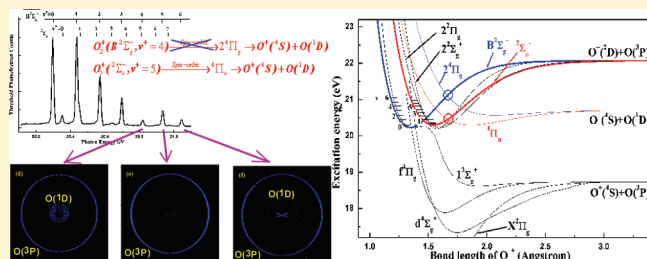
1. INTRODUCTION

Photoelectron−photoion coincidence (PEPICO) technique, as a powerful approach to produce and study state-selected ions, has been applied for a long time.[1,2] In principle, the kinetic energy of the photoelectron is correlated with the internal energy of its coincident ion when a molecule is photoionized. If only the photoelectrons with zero kinetic energies are detected, this type of PEPICO method is usually called as threshold PEPICO (TPEPICO).[3−13] It is well-known that the TPEPICO method has the advantages of higher collection efficiency and higher energy resolution of photoelectrons.

In most of the TPEPICO experiments,[3,7−11,14−20] linear and/ or reflectron time-of-flight (TOF) mass spectrometers were employed to detect ions. When the internal energies of ions exceed dissociation limits, dissociative photoionization (DPI) processes will occur. In this case, fragment ions are usually produced with kinetic energies, and hence their TOF profiles in mass spectra are broadened. Through fitting the TOF profiles of fragments, kinetic energy released distribution (KERD) in dissociation can be obtained.[14−18,21−24] However, its energy resolution is generally limited, and thereby some delicate information in dissociation may be buried.

Compared with the method of fitting TOF profiles, velocity map imaging (VMI)[25] can provide not only the highly resolved KERD, but also the angular distribution simultaneously. Thus, we have constructed a novel TPEPICO mass spectrometer with double VMI using synchrotron radiation (SR),[12] in which a delicate VMI design has been applied for both photoelectrons

and photoions simultaneously. Benefiting from the application of VMI, threshold photoelectrons (TPEs) can be detected with the higher collection efficiency and higher energy resolution. From the VMI of photoions in coincidence with the TPEs, the KERD and angular distributions can be measured directly, and then the dissociation mechanisms and dynamics of state-specified molecular ions can be obtained.

As a simple diatomic molecule, the electronic configuration of the ground state oxygen molecule is $(1\sigma_g)^2(1\sigma_u)^2(2\sigma_g)^2(2\sigma_u)^2$-$(3\sigma_g)^2(1\pi_u)^4(1\pi_g)^2$. When an electron is excited from the $3\sigma_g$ bonding orbital and taken out, the oxygen molecule will be ionized to form the O_2^+ ion at $B^2\Sigma_g^-$ or $b^4\Sigma_g^-$ state.[26,27] The $B^2\Sigma_g^-$ state is strongly predissociative, and its ionic structure was explored by He I(II) photoelectron,[28] TPE,[29−31] TPEPICO,[14,32−36] and pulsed field ionization photoelectron (PFI-PE) spectroscopy.[37] Two dissociation channels exist in the excitation energy range of the $B^2\Sigma_g^-(v^+ = 0{-}6)$ states, i.e., the first limit of $O^+(^4S) + O(^3P)$ at 18.733 eV and the second limit of $O^+(^4S) + O(^1D)$ at 20.700 eV.[32−34] The corresponding dissociation dynamics were investigated using the TPEPICO method,[32−35] in which the KERDs of fragment ions and the predissociative lifetimes of different vibrational states were roughly obtained. Recently, the dissociation of the $B^2\Sigma_g^-$ state has also been studied by the vector-correlation method.[38] However, the vibrational levels of $B^2\Sigma_g^-$ are

not well resolved in the vector-correlation measurement due to the limited energy resolution.

Although numerous experimental studies have been done before, the angular distributions of the O^+ fragment ions from $O_2^+(B^2\Sigma_g^-)$ states and the corresponding dissociation mechanisms are still not very clear. In this work, we performed TPEPICO velocity imaging experiments to reinvestigate dissociation of the vibrational state-selected $O_2^+(B^2\Sigma_g^-)$ ions. The TPEPICO velocity images of the O^+ fragment ions were presented, and both the speed and angular distributions were obtained subsequently. In addition, the relationships between the branching ratios of two dissociation channels with the excited vibronic levels were discussed and a new predissociation mechanism was suggested.

2. EXPERIMENTS

The present TPEPICO imaging experiments were performed at the U14-A beamline of the National Synchrotron Radiation Laboratory (Hefei, China). The details of the beamline have been introduced previously,[12,39] and thus it is only described briefly here. SR from an undulator was dispersed with a 6 m spherical-grating monochromator equipped with three gratings (370, 740, or 1250 grooves·mm^{-1}). In the present experiments, only the 370 grooves·mm^{-1} grating was used to cover the photon energy from 7.5 to 22.5 eV. The energy resolution was about 2000 when the widths of the entrance and exit slits of the monochromator were set as 80 μm. The absolute photon energy scale of the grating was carefully calibrated using the well-known ionization energies of gases. Using five spectral lines at 21.565 (Ne), 18.355 (N$_2$), 15.760 (Ar), 14.000 (Kr), and 12.120 eV (Xe), the relations between wavelength and position of the grating were determined precisely. A gas filter filled with neon gas was placed in front of the photoionization chamber to eliminate higher order harmonic radiation of the undulator.

Photoelectrons and photoions were collected through a specially designed ion lens, and their velocity images were mapped at opposite direction simultaneously.[12] A significant improvement of suppression of hot electrons was acquired by utilizing a repelling VMI electric field to magnify the image of photoelectrons.[12,40] A single-start/multiple-stop (SM) data acquisition mode[41] was utilized to record TPEPICO TOF mass spectra, where TPEs provided start signals for measuring TOFs of ions. Through the VMI electric field, photoions were accelerated and projected onto a dual microchannel plate (MCP) backed by a Phosphor Screen (Burle Industries, P20). A TE-cooling CCD detector (Andor, DU934N−BV) was used to record images on the screen. Since the electric vector of SR light was perpendicular to the axis of the TOF tube and parallel to the surface of MCP, the three-dimensional (3D) image of ions could be obtained from inverse Abel transformation of two-dimensional raw image,[25] or directly from the time-sliced image.[12,42]

A continuous supersonic molecular beam of pure O$_2$ gas was generated through a 30 μm diameter nozzle with a stagnation pressure of 1.1 atm. The molecular beam was collimated by a 0.5 mm diameter skimmer and then intersected by SR at 10 cm downstream from the nozzle. The source chamber and ionization chamber of the coincidence imaging spectrometer were pumped respectively by the 1800 and 1600 L/s turbomolecular pumps, and the typical backing pressures were 2×10^{-3} Pa and 4×10^{-5} Pa with the molecular beam on. The signal intensities of detected electrons and ions were normalized using the photon flux from a
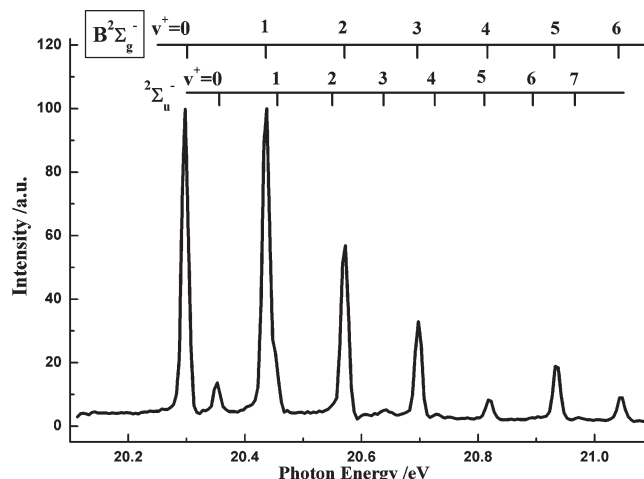

Figure 1. TPES of O$_2$ in the energy range of 20.1−21.1 eV. The vibrational progressions of the B$^2\Sigma_g$ and $^2\Sigma_u$ states were assigned respectively.

Table 1. Ionization Energies and Relative Intensities of Vibronic Levels of O$_2^+$ (B$^2\Sigma_g^-$, $^2\Sigma_u^-$)

assignment	ionization energy (eV)			relative intensity		
	TPES^a	TPES^b	PFI-PES^c	TPES^a	TPES^b	PFI-PES^c
B$^2\Sigma_g^-$ v$^+$=0	20.298	20.296	20.2983	99.8	108.0	94.1
$^2\Sigma_u^-$ v$^+$=0	20.353	20.352	20.3528	13.6		
B$^2\Sigma_g^-$ v$^+$=1	20.438	20.436	20.4361	100.0	100.0	100.0
$^2\Sigma_u^-$ v$^+$=1	20.453^d	20.449	20.4518			
$^2\Sigma_u^-$ v$^+$=2	20.553^d		20.5488			
B$^2\Sigma_g^-$ v$^+$=2	20.573	20.565	20.5690	56.8	85.0	53.8
$^2\Sigma_u^-$ v$^+$=3	20.638	20.637	20.6392	5.2		
B$^2\Sigma_g^-$ v$^+$=3	20.697	20.691	20.6958	32.9	44.0	31.2
$^2\Sigma_u^-$ v$^+$=4	20.727	20.725	20.7281	5.8		
$^2\Sigma_u^-$ v$^+$=5	20.817^d		20.8106			
B$^2\Sigma_g^-$ v$^+$=4	20.817	20.812	20.8180	8.2	11.1	6.2
$^2\Sigma_u^-$ v$^+$=6	20.897^d		20.8936			
B$^2\Sigma_g^-$ v$^+$=5	20.932	20.927	20.9349	18.9	26.6	17.4
$^2\Sigma_u^-$ v$^+$=7	20.972^d		20.9721			
B$^2\Sigma_g^-$ v$^+$=6	21.042	21.038	21.0470	9.0	10.8	11.9

^{a} Present experimental results, where the ionization energies were read from the peak positions and the relative intensities were estimated from the peak heights of TPES in Figure 1. ^{b} Data from ref 30. ^{c} Data from ref 37. ^{d} Resonance energies were estimated based on the present TPES and previous PFI-PES.

silicon photodiode (International Radiation Detectors Inc., SXUV-100).[12]

3. RESULTS AND DISCUSSION

3.1. Threshold Photoelectron Spectrum (TPES) of O$_2$ in the Energy Range of 20.1−21.1 eV. TPES of O$_2$ in the excitation energy range of 20.1−21.1 eV was measured with a step size of 5 meV, and presented in Figure 1, where the main resonance structures of the spectrum were very similar to the previous measurements.[28−31,34,36,37] According to the assignment of Evans et al.,[37] the vibrational progress (v^+ = 0−6) of
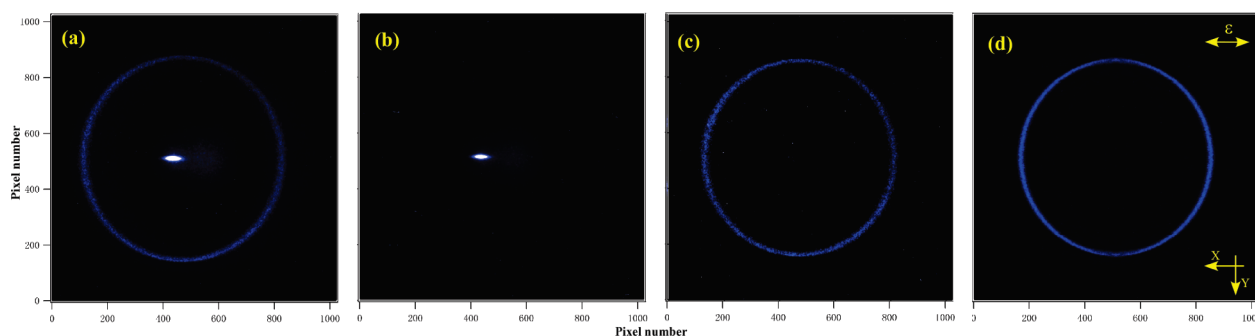
Figure 2. Time-sliced coincidence images from the dissociation of $O_2^+(B^2\Sigma_g^-, v^+ = 0)$ state. (a) Raw image of O^+. (b) Raw image contributed by the false coincidence events. (c) Modified coincidence image of O^+ after subtracting image b from image a; (d) Modified image after deconvolution, quadrant symmetrization, and moving to the center of image.

the $B^2\Sigma_g^-$ state and several vibronic bands of the concomitant $^2\Sigma_u^-$ state were clearly observed in the present energy range.

The ionization energies and relative intensities of the vibronic levels of $O_2^+(B^2\Sigma_g^-, ^2\Sigma_u^-)$ observed in the present experiments are summarized in Table 1, as well as the previous TPES[30] and PFI-PES[37] data. Obviously, the present ionization energies agreed well with the previous results, where the differences were less than 5 meV and within the energy uncertainty of the grating (~10 meV). Moreover, the relative intensities of vibrational bands in the present TPES were very similar to those of the PFI-PES,[37] but a little difference existed between our data and the previous TPES.[30] As hot electrons are suppressed more efficiently in our spectrometer,[12] the present intensities were believed to be more reliable. In addition, the intensities of $v^+ = 5$ and 6 vibrational bands in TPES were higher than that of the $v^+ = 4$ band, which is thought to be due to the enhancement effect of near resonant autoionization.[37]

3.2. TPEPICO-TOF Mass Spectrum for the $O_2^+(B^2\Sigma_g^-)$ State. Two dissociation limits for O_2^+ are involved in the present excitation energy range: $O^+(^4S)+O(^3P)$ at 18.733 eV and $O^+(^4S)+O(^1D)$ at 20.700 eV.[32−35] When fixing the photon energy at 20.298 eV of the $O_2^+(B^2\Sigma_g^-, v^+ = 0)$ state, only the first dissociation limit can be reached, and the O_2 molecules undergo a DPI process to produce $O^+(^4S)$ fragment ions. With a 25 V· cm^{-1} extraction electric field in the ionization region, a nearly rectangle-shape TOF profile was observed in the present TPE-PICO TOF mass spectrum to cover the 6.05−6.55 μs range with a center of 6.30 μs, whose spectral carrier was definitely assigned to the O^+ fragment ions. Due to the released kinetic energy in dissociation, the total TOF width of O^+ expanded to about 500 ns. For all vibrational bands of the $B^2\Sigma_g^-$ state, the measured mass spectra were very similar to those of Richard-Viard et al.,[34] except that almost no TOF peak for O_2^+ ions was observed in the present measurement. Because the $B^2\Sigma_g^-$ electronic state of O_2^+ is fully predissociative, the mass peak of O_2^+ (centered at 8.9 μs) should not be observed in the TPEPICO TOF mass spectra. Therefore, the TOF peak of O_2^+ observed by Richard-Viard et al.[34] should come from the false coincidence events. With the vibrational excitation, the TOF widths of the O^+ fragment were expanded a bit, and a second component with lower kinetic energy appeared at the $v^+ = 4$ level. Interestingly, this second component abruptly disappeared at $v^+ = 5$, which was consistent with the previous measurements;[32−35] however, it regenerated at the $v^+ = 6$ level.

3.3. TPEPICO Images of O^+ Ions Dissociated from O_2^+ $(B^2\Sigma_g^-, v^+ = 0−6)$. In the present experiments, the 3D time-sliced

imaging method was used to record the TPEPICO images of O^+ fragments, in which a pulsed high voltage triggered by the collected TPEs was applied to ion MCPs as a mass gate to select O^+.[12] The typical mass gate was located at the O^+ TOF center of 6.30 μs and with 80 ns duration.

The recorded raw coincidence velocity image of O^+ fragment ions dissociated from the $O_2^+(B^2\Sigma_g^-, v^+ = 0)$ state was presented in Figure 2a. The molecular beam flowed along the x-axis direction from right to left, and the vacuum ultraviolet (VUV) light propagated along the y-axis with the electric field vector ε along the x-axis in this configuration. There were obviously three components in Figure 2a: an outer ring, an excenric bright spot, and a weak middlemost diffuse plaque. As we discussed previously,[12] both the ring and the bright spot are off the center of the image and correspond to the flowing downstream distance of ions with a certain center-of-mass (CM) speed along the x-axis. Moreover, the center of the ring does not coincide with the bright spot, indicating their spectral carriers are totally different. Because only the first dissociation limit $O^+(^4S) + O(^3P)$ at 18.733 eV can be reached at the present excitation energy, the coincident O^+ fragment ions had a certain kinetic energy, and thereby contributed to the outer ring of the image. As noted in ref 12, the O_2^+ parent ions generated in the false coincidence events distribute randomly in time, and thus they can be collected partially in the mass gate as well and contribute the bright spot. Therefore, combining the flowing downstream distance of the bright spot and the O_2^+ flight time, the CM speed of the present molecular beam was calculated to be about 732 m·s^{-1}. The parallel translational temperature of beam was calculated to be 27 K by fitting the x-axis intensity distribution of the O_2^+ image (bright spot) in Figure 2a with a Gaussian function.[43] Additionally, the middlemost diffuse plaque was believed to come from the contribution of background ions in the chamber,[44] as it still existed with the molecular beam off.

Generally, the speed distribution of O^+ fragment ions could be obtained directly by accumulating intensities of the outer ring in the image. However, the excenric bright spot and the middlemost diffuse plaque would cause errors in accumulating process, especially for the lower speed distribution (close to the center of image). As the false coincident ions distribute uniformly in the present TPEPICO TOF mass spectra when the average ionization frequency is kept less than 1 kHz,[12] we chose an "empty" mass gate (a time center of 2.0 μs and 80 ns duration) and recorded its image, which corresponded to the false coincidence ions and is shown in Figure 2b. Obviously, the bright spot and diffuse plaque in the image are identical with those in Figure 2a.
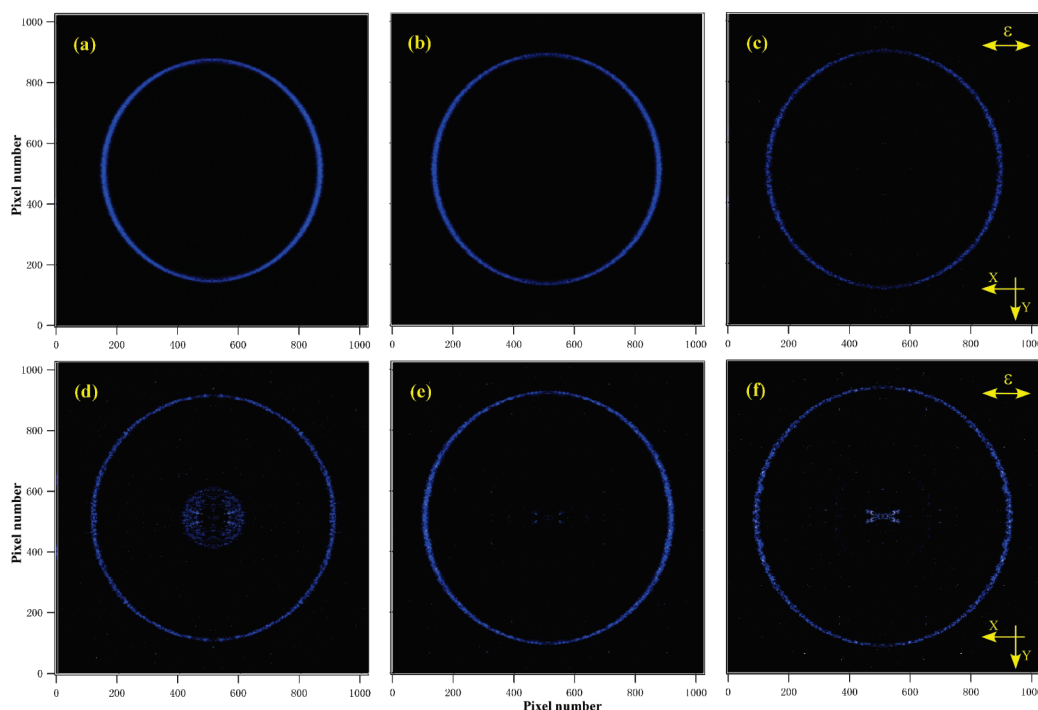
Figure 3. The modified coincidence O^+ fragment ion images from the $O_2^+(B^2\Sigma_g^-, v^+ = 1-6)$ state, where panels a−f are recorded at 20.438, 20.573, 20.697, 20.817, 20.932, 21.042 eV, respectively, and correspond to the $v^+ = 1-6$ vibrational states.

Consequently, the pure coincidence image from the $O_2^+(B^2\Sigma_g^-, v^+=0)$ state was obtained by subtracting Figure 2b from Figure 2a and presented in Figure 2c. Only the outer ring remained in the modified coincidence image of Figure 2c, and its shape and intensity were kept, indicating that contribution from the false coincidence events in the raw TPEPICO image was eliminated.

As mentioned above, the parallel translational temperature of the molecular beam was 27 K, and thus the speed distribution of the molecular beam along the x-axis can cause the width of the rings in the images to slightly broaden along the direction as shown in Figure 2c.[12,25] A Gaussian profile could be used to fit the intensity distribution along the x-axis of the bright spot (false coincident parent ions) in the image of Figure 2b, which represented the speed distribution of the beam along this direction. Consequently, the true intensity distribution in the coincidence image of O^+ could be obtained through deconvolution with the fitted Gaussian function. In addition, the coincidence images also need be further processed with quadrant symmetrization to reduce nonuniformity of the MCP detector. The details of this multistep data disposure process are described in the Supporting Information of ref 45. Finally the modified coincidence images of the O^+ fragment ions dissociated from $O_2^+(B^2\Sigma_g^-, v^+ = 0)$ are exhibited in Figure 2d. Similarly, the coincidence 3D velocity images of the O^+ fragment ions from the other vibronic levels $(B^2\Sigma_g^-, v^+ = 1-6)$ were processed with the same approach and are shown in Figure 3. In the following sections, only the modified coincidence images are presented and discussed unless otherwise noted.

With the vibrational quantum number increasing, the diameter of the ring increased gradually. It is well-known that only two dissociation limits, $O^+(^4S) + O(^3P)$ at 18.733 eV, and $O^+(^4S) + O(^1D)$ at 20.700 eV can be achieved in the present excitation energy range. When the photon energy reaches 20.817 eV of the $B^2\Sigma_g^-(v^+ = 4)$ energy level, a second ring with a smaller diameter

appeared in the image as shown in Figure 3d. Therefore, two rings in the image straightforwardly corresponded to the two dissociation channels, respectively. The outer ring was contributed by the O^+ ions dissociated along the lower dissociation pathway of $O^+(^4S) + O(^3P)$, while the inner ring corresponded to the $O^+(^4S) + O(^1D)$ dissociation channel. Interestingly, the inner ring in the modified coincidence image of the $O_2^+(B^2\Sigma_g^-, v^+ = 5)$ state of Figure 3e was very weak, implying that almost all the $O_2^+(B^2\Sigma_g^-, v^+ = 5)$ ions dissociated along the lower channel to produce $O^+(^4S)$ fragment ions. Nevertheless, when the photon energy was increased to 21.042 eV of the $B^2\Sigma_g^-(v^+ = 6)$ level, the inner ring reappeared in the image as shown in Figure 3f.

3.4. Speed Distributions of O^+ Fragment Ions. From the modified coincidence images of O^+ in Figure 2d and Figure 3, the speed distributions of the O^+ fragment were derived directly by integrating the intensity of the image over angles,[45] and are presented in Figure 4.

A unique peak was observed in the speed distribution for $v^+ = 0-3$, while an additional peak distinctly appeared for $v^+ = 4$ and 6 levels. For the $v^+ = 5$ level, the second speed distribution around 1200 m·s^{-1} was almost nonexistent. The magnitudes of speed gradually increased with the vibrational number. As mentioned above, the higher speed distribution in Figure 4 corresponded to the first dissociation channel of $O^+(^4S) + O(^3P)$, and the lower speed peaks with a weaker intensity correlated to the second dissociation pathway of $O^+(^4S) + O(^1D)$. The obtained speed distributions of O^+ fragment ions from different vibrational states were summarized in Table 2, which exactly match the images in Figures 2d and 3. It should be noted that the speed distributions of the $O(^1D)$ channel showed an elongated shape toward lower speeds, which were different with the symmetric profiles of the $O(^3P)$ speed distributions. Generally, a sufficiently narrow mass gate is necessary to record the 3D time-sliced image and obtain the same speed distribution as the conventional

velocity imaging. However, the TOF widths of the O^+ fragment associated with the $O(^1D)$ channel only expanded a little bit, and thereby the time-sliced images did not present good resolution for the inner images in Figure 3d–f. With the same data disposure process as the outer ring, the obtained speed distributions of the $O(^1D)$ channel showed an asymmetric profile with a tail toward lower speeds.

From the energy conservation and momentum conservation, the speed of O^+ fragment ions, V_{O+}, can be calculated from the relation

$$h\nu - D_0 = E_{\text{total}} = 2E_{O^+} = m_{O^+}V_{O^+}^2 \qquad (1)$$

where $h\nu$ is the excitation photon energy, D_0 is the dissociation limit for a specific channel, E_{total} is the total released kinetic energy, m_{O+} and V_{O+} are the mass and speed of the O^+ fragment ion, respectively. Taking the dissociation limits D_0 as 18.733 eV for the $O^+(^4S) + O(^3P)$ channel and 20.700 eV for the $O^+(^4S) + O(^1D)$ channel,[34] the speeds of the O^+ fragment ions from dissociation of the $O_2^+(B^2\Sigma_g^-, v^+ = 0-6)$ levels were calculated and listed in Table 2 as well. Obviously, the present experimental and calculated speeds agreed very well, and the errors of less than 20 m·s^{-1} corresponded to about 8 meV energy, which mostly came from the energy uncertainty of the grating.

3.5. Branching Ratio Dependent on Vibrational States and Predissociation Mechanism. From Figures 3 and 4, an abrupt
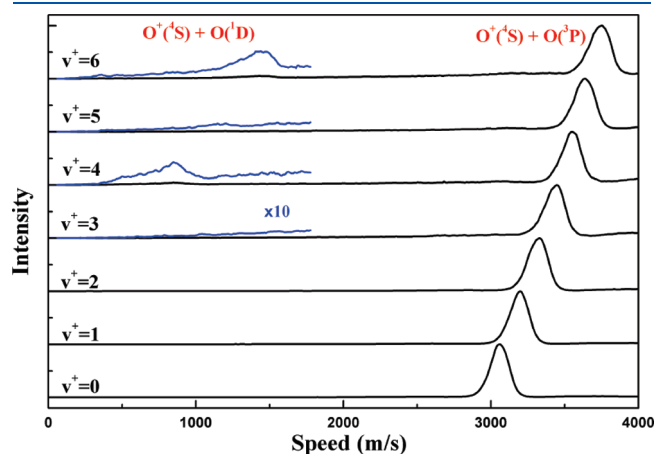

Figure 4. Speed distributions of the O^+ fragment from dissociation of $O_2^+(B^2\Sigma_g^-, v^+ = 0-6)$ ions.

variation of branching ratio for the two dissociation channels could be observed with the vibronic levels. As a strongly predissociative state, the $O_2^+(B^2\Sigma_g, v^+ = 0-3)$ states can dissociate completely along the lower channel $O^+(^4S) + O(^3P)$. The potential energy curves of the low-lying electronic states of O_2^+ from Beebe et al.'s calculations are shown in Figure 5,[26] which are obtained by reading points of the enlarged copy of the published figures. For all listed electronic states, the calculated energy difference between the states remains good for spectroscopic data, thus these calculated curves are generally used to analyze ionization/dissociation mechanisms up to now,[32–35,46] although an energy shift exists between experimental and calculated dissociation limits. In order to match the experimental dissociation limits, we slightly vertically shifted the calculated curves in Figure 5.

On the basis of the calculated potential energy curves, the $1^2\Sigma_g^+$ state was the best candidate to intersect the $B^2\Sigma_g$ state to cause predissociation, while the $f^4\Pi_g$ and $d^4\Sigma_g^+$ states cross the $B^2\Sigma_g$ state near its equilibrium distance and probably caused its predissociation as well.[34] All these interactions could make the $B^2\Sigma_g$ state dissociate along the lowest $O^+(^4S) + O(^3P)$ dissociation pathway.

When the photon energy increased to over the second dissociation limit of $O^+(^4S) + O(^1D)$, the O^+ fragment ions could be produced via both channels, although the lower $O^+(^4S) + O(^3P)$ channel was kept dominant. Accumulating intensities of the higher and lower speed components in Figure 4, the branching ratio of two dissociation channels could be estimated for the $v^+ = 4$ and 6 levels. Nearly 10% of the O_2^+ ions dissociated along the second dissociation pathway of $O^+(^4S) + O(^1D)$ for both the $v^+ = 4$ and 6 states, while no O^+ fragment ions corresponding to the second dissociation channel were observed for the $v^+ = 5$ level. Previous experiments[32–35] have mentioned a similar phenomena through fitting the TOF profile of O^+, although no TOF profiles of O^+ for $v^+ = 5$ and 6 states have been displayed in the published papers. The present images intuitively showed this vibrational dependency, and were consistent with the previous conclusions. However, there was no satisfactory explanation for the fluctuation of the branching ratios with the vibronic levels up to now.[32–35]

As Beebe et al. calculated, the second dissociation pathway can be performed through crossing between the $2^4\Pi_g$ and $B^2\Sigma_g$ states at an energy around the $B^2\Sigma_g(v^+ = 6)$ level.[26] Marian et al.[47] recalculated these potential energy curves and found this

Table 2. Speed Distributions and Anisotropic Parameters (β) of the O^+ Fragment Ions from Dissociation of State-Selected $O_2^+(B^2\Sigma_g^-, v^+ = 0-6)$ Ions

			speed of O^+ /m·s^{-1}		β		
v^+	$h\nu$ /eV	dissociation channel	exp.	cal.	present	previous[a]	τ /ps[b]
0	20.298	$O^+(^4S) + O(^3P)$	3055 ± 10	3072	0.20 ± 0.07	0.25 ± 0.17	0.90
1	20.438	$O^+(^4S) + O(^3P)$	3197 ± 10	3205	0.28 ± 0.07	0.24 ± 0.17	0.45
2	20.573	$O^+(^4S) + O(^3P)$	3330 ± 10	3328	0.34 ± 0.07	0.26 ± 0.19	0.45
3	20.697	$O^+(^4S) + O(^3P)$	3446 ± 10	3441	0.25 ± 0.07	0.19 ± 0.20	0.80
4	20.817	$O^+(^4S) + O(^3P)$	3552 ± 10	3546	0.16 ± 0.08	0.19 ± 0.20	0.50
		$O^+(^4S) + O(^1D)$	853 ± 10	844	0.19 ± 0.09		
5	20.932	$O^+(^4S) + O(^3P)$	3632 ± 10	3644	0.29 ± 0.07	0.16 ± 0.17	0.50
6	21.042	$O^+(^4S) + O(^3P)$	3756 ± 10	3736	0.25 ± 0.08		0.75
		$O^+(^4S) + O(^1D)$	1439 ± 10	1447	0.09 ± 0.09		

[a] Reference 47. [b] Lifetime of individual vibronic levels from ref 37.

6343

dx.doi.org/10.1021/jp111590s | *J. Phys. Chem. A* 2011, 115, 6339–6346

Figure 5. The modified potential energy curves of the low-lying electronic states of O_2^+ from ref 26.

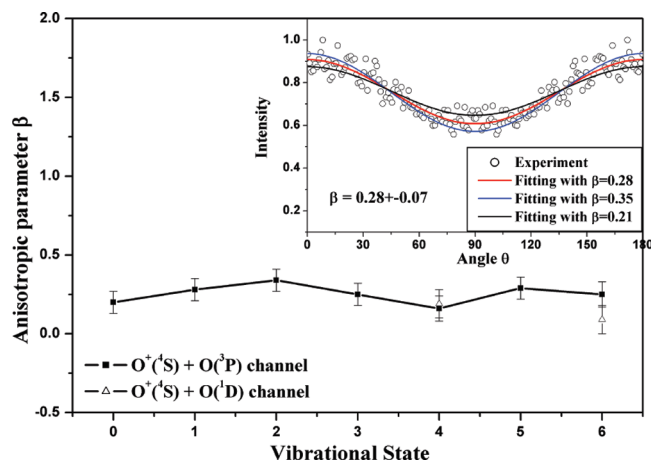**Figure 6.** Anisotropic parameters of dissociation from $O_2^+(B^2\Sigma_g^-, v^+ = 0-6)$ states. The experimental and fitted angular distributions of O^+ fragment ions dissociated from $O_2^+(B^2\Sigma_g, v^+ = 1)$ states are presented in the inset, where the open circles represent experimental data and the solid lines are the fitted curves.

intersection in the neighborhood of $v^+ = 10$. Since the dissociation limits calculated by Beebe et al. were more consistent with the experimental data, their potential energy curves of the low-lying electronic states of O_2^+ were generally quoted in refs 32−35 and 46. Thus we also used Beebe et al.'s curves to discuss the dissociation mechanism of the $B^2\Sigma_g^-$ state.

In experiments, the second dissociation channel was found to be open at the $B^2\Sigma_g^-(v^+ = 4)$ level, implying that the intersection was probably lower than the calculated value.[32] However, this reason can not explain the abrupt decrease of the branching ratio of the $O(^1D)$ channel at the $B^2\Sigma_g^-(v^+ = 5)$ level. Another explanation is suggested by Richard-Viard et al. as indirect predissociation via an intermediate state $(2^2\Pi_g$ or $2^2\Sigma_g^+)$.[34] Since the $2^2\Pi_g$ or $2^2\Sigma_g^+$ states adiabatically correlate to the third dissociation limits $(O^+(^2D) + O(^3P))$, the second-step crossing between this intermediate state with $2^4\Pi_g$ is necessary to produce $O^+(^4S) + O(^1D)$ after the initial incidental resonance between $B^2\Sigma_g^-(v^+ = 4)$ with a certain vibronic level of $2^2\Pi_g$ or $2^2\Sigma_g^+$ states. Because the intersection between the $B^2\Sigma_g^-$ and $2^2\Pi_g$ (or $2^2\Sigma_g^+$) states is far lower in energy than the $B^2\Sigma_g^-(v^+ = 4)$ level, a similar incidental resonance between $B^2\Sigma_g^-(v^+ = 5)$ and the vibronic level of $2^2\Pi_g$ or $2^2\Sigma_g^+$ states should exist as well, and thereby an indirect predissociation is also expected for O_2^+-$(B^2\Sigma_g^-, v^+ = 5)$, which is contrary to the experimental conclusions.

In a recent spectral assignment of PFI-PES by Evans et al.,[37] a vibrational progress of the concomitant $^2\Sigma_u^-$ state is first confirmed in the excitation energy range through simulating the rotational structure. Specifically, the $^2\Sigma_u^-(v^+ = 5)$ and $B^2\Sigma_g^-(v^+ = 4)$ levels have very close ionization energies within the present energy uncertainty of 10 meV, as shown in Table 1. Therefore, a new predissociation mechanism for the appearance of the second dissociation channel at the $B^2\Sigma_g^-(v^+ = 4)$ level could be suggested, in which both the $B^2\Sigma_g^-(v^+ = 4)$ and $^2\Sigma_u^-(v^+ = 5)$ states are simultaneously populated at 20.817 eV, and then the coupling between the $^2\Sigma_u^-(v^+ = 5)$ and nearby $^4\Pi_u$ states caused the predissociation to form $O^+(^4S)$ and $O(^1D)$ fragments. Since the intersection between the $^2\Sigma_u^-$ and $^4\Pi_u$ states, as noted with a red circle in Figure 5, existed at a lower energy than the crossing point of the $B^2\Sigma_g^-$ and $2^4\Pi_g$ states (blue circle), the second dissociation channel seemed to be open at the $B^2\Sigma_g^-(v^+ = 4)$ level (20.817 eV). When the ionization energy was increased to the $B^2\Sigma_g^-(v^+ = 5)$ level, the $O^+(^4S) + O(^1D)$ dissociation limit could

not be reached because the incidental degeneration between the $B^2\Sigma_g^-(v^+ = 5)$ and $^2\Sigma_u^-$ states does not exist yet, and the energy is still lower than the intersection of $B^2\Sigma_g^-$ and $2^4\Pi_g$ states. Subsequently, the second dissociation channel reappeared once the excitation energy was beyond the intersection between $B^2\Sigma_g^-$ and $2^4\Pi_g$ states, e.g., at the $B^2\Sigma_g^-(v^+ = 6)$ level. Therefore, the predissociation mechanism was more reliable and able to distinctly explain the vibrational dependency of the branching ratio of the two dissociation channels.

3.6. Angular Distributions of O^+ Fragment Ions. From the modified coincidence images in Figures 2d and 3, angular distributions of O^+ fragment ions can be derived by integrating over a proper range of speed at each angle. Consequently, the anisotropy parameter β can be obtained by fitting the angular distribution, $I(\theta)$, with the formula[48]

$$I(\theta) = (4\pi)^{-1}[1 + \beta \cdot P_2(\cos\theta)] \qquad (2)$$

where θ is the angle between the recoil velocity of fragment ions and the electric field vector ε of VUV light, and $P_2(\cos\theta)$ is the second-order Legendre polynomial. Figure 6 shows the dependence of the anisotropic parameters β on the v^+ number. To compare the present and previous conclusions, the fitted values of β together with the previous data derived from fitting TOF profiles[49] are summarized in Table 2. As an example, both the experimental data and fitted angular distributions of O^+ fragment dissociated from $O_2^+(B^2\Sigma_g^-, v^+ = 1)$ states are presented in the inset of Figure 6. Obviously, the uncertainties of the β values obtained from the images were much smaller than those of previous fitting results. The present β values were consistent with the lifetimes obtained by Evans et al.[37] All the β values were near zero, indicating that the O^+ fragment ions from $O_2^+(B^2\Sigma_g^-, v^+ = 0-6)$ states had a nearly isotropic distribution in dissociation. Therefore, the dissociation of $O_2^+(B^2\Sigma_g^-, v^+ = 0-6)$ states were really predissociative on a time scale that was much slower than that of molecular rotation.

4. CONCLUSIONS

Dissociation of vibrationally selected $O_2^+(B^2\Sigma_g^-, v^+ = 0-6)$ states in the 20.1−21.1 eV energy range were studied using

6344

dx.doi.org/10.1021/jp111590s |*J. Phys. Chem. A* 2011, 115, 6339–6346

TPEPICO velocity imaging. The ionization energies and relative intensities in the present TPES were reasonably consistent with previous results. The 3D coincidence velocity images of O^+ fragment ions dissociated from the $O_2^+(B^2\Sigma_g^-, v^+ = 0-6)$ states were measured for the first time.

In the present experiments, an improvement was applied for acquiring the pure TPEPICO images through subtracting an image of the false coincident ions from the recorded raw TPEPICO images, and thus the influences of the false coincidence events in images could be eliminated. Consequently, speed and angular distributions of the O^+ fragment ions were obtained for every vibrational state of $O_2^+(B^2\Sigma_g^-)$. The anisotropic parameters of the O^+ fragment ions from different dissociation channels were determined through fitting the angular distributions. All anisotropic parameters were found to be close to zero, indicating that all the $O_2^+(B^2\Sigma_g^-, v^+ = 0-6)$ states predissociated on a time scale that was much slower than that of molecular rotation.

Interestingly, the branching ratios of the O^+ ions produced along the two dissociation pathways showed a dramatic variation with the v^+ quantum number. Nearly 10% of the O_2^+ ions dissociated along the second dissociation pathway of $O^+(^4S) + O(^1D)$ for both the $v^+ = 4$ and 6 states, while no O^+ fragment ions corresponding to the $O(^1D)$ dissociation channel were observed for the $v^+ = 5$ level. A new reasonable explanation was suggested, in which the $B^2\Sigma_g^-(v^+ = 4)$ and concomitant $^2\Sigma_u^-(v^+ = 5)$ states are populated simultaneously at 20.817 eV, and then the coupling between $^2\Sigma_u^-(v^+ = 5)$ and nearby $^4\Pi_u$ states caused predissociation to form $O^+(^4S)$ and $O(^1D)$. When the ionization energy was increased to the $B^2\Sigma_g^-(v^+ = 5)$ level, the $O^+(^4S) + O(^1D)$ dissociation limit could not be reached because the incidental degeneration did not exist, and the excitation energy was still lower than the intersection of $B^2\Sigma_g^-$ and $2^4\Pi_g$ states. Subsequently, the second dissociation pathway reappeared once the excitation energy was increased to the $B^2\Sigma_g^-(v^+ = 6)$ level and beyond the intersection of $B^2\Sigma_g^-$ and $2^4\Pi_g$ states.

■ AUTHOR INFORMATION

Corresponding Author
*E-mail: xzhou@ustc.edu.cn.

■ REFERENCES

(1) Brehm, B.; Puttkamer, E. V. Koinzidenzmessung von photoionen und photoelektronen bei methan. *Z. Naturforsch.* **1967**, *22A*, 8.
(2) Eland, J. H. D. Photoelectron—photoion coincidence spectroscopy. I. Basic principles and theory. *Int. J. Mass Spectrom. Ion Phys.* **1972**, *8* (2), 143–151.
(3) Stockbauer, R. Threshold electron—photoion coincidence mass-spectrometric study of CH₄, CD₄, C₂H₆, and C₂D₆. *J. Chem. Phys.* **1973**, *58* (9), 3800–3815.
(4) Baer, T., State selection by photoion—photoelectron coincidence. In *Gas Phase Ion Chemistry*; Bowers, M. T., Ed.; Academic Press: New York, 1979; pp 153–196.

(5) Baer, T. Vacuum UV photophysics and photoionization spectroscopy. *Annu. Rev. Phys. Chem.* **1989**, *40*, 637–669.
(6) Ng, C. Y. *Vacuum Ultraviolet Photoionization and Photodissociation of Molecules and Clusters*; World Scientific: Singapore, 1991.
(7) Holland, D. M. P.; Shaw, D. A.; Sumner, I.; Hayes, M. A.; Mackie, R. A.; Wannberg, B.; Shpinkova, L. G.; Rennie, E. E.; Cooper, L.; Johnson, C. A. F.; Parker, J. E. The design and performance of a threshold-photoelectron—photoion coincidence spectrometer for the study of unimolecular decomposition in polyatomic ions. *Nucl. Instrum. Methods Phys. Res., Sect. B* **2001**, *179* (3), 436–454.
(8) Sztaray, B.; Baer, T. Suppression of hot electrons in threshold photoelectron photoion coincidence spectroscopy using velocity focusing optics. *Rev. Sci. Instrum.* **2003**, *74* (8), 3763–3768.
(9) Baer, T.; Sztaray, B.; Kercher, J. P.; Lago, A. F.; Bodi, A.; Skull, C.; Palathinkal, D. Threshold photoelectron photoion coincidence studies of parallel and sequential dissociation reactions. *Phys. Chem. Chem. Phys.* **2005**, *7* (7), 1507–1513.
(10) Garcia, G. A.; Soldi-Lose, H.; Nahon, L. A versatile electron—ion coincidence spectrometer for photoelectron momentum imaging and threshold spectroscopy on mass selected ions using synchrotron radiation. *Rev. Sci. Instrum.* **2009**, *80* (2), 023102.
(11) Bodi, A.; Johnson, M.; Gerber, T.; Gengeliczki, Z.; Sztaray, B.; Baer, T. Imaging photoelectron photoion coincidence spectroscopy with velocity focusing electron optics. *Rev. Sci. Instrum.* **2009**, *80* (3), 034101.
(12) Tang, X. F.; Zhou, X. G.; Niu, M. L.; Liu, S. L.; Sun, J. D.; Shan, X. B.; Liu, F. Y.; Sheng, L. S. A threshold photoelectron—photoion coincidence spectrometer with double velocity imaging using synchrotron radiation. *Rev. Sci. Instrum.* **2009**, *80* (11), 113101.
(13) Baer, T.; Dunbar, R. C. Ion Spectroscopy: Where did it come from; where is it now; and where is it going? *J Am. Soc. Mass. Spectrom.* **2010**, *21* (5), 681–693.
(14) Guyon, P. M.; Baer, T.; Ferreira, L. F. A.; Nenner, I.; Tabchefouhaile, A.; Botter, R.; Govers, T. R. Observation of dissociative states of O₂⁺ by threshold photoelectron—photoion coincidence. *J. Phys. B: At., Mol. Opt. Phys.* **1978**, *11* (5), L141–L144.
(15) Boyle, K. J.; Jarvis, G. K.; Tuckett, R. P. Threshold photoelectron spectroscopy of PX₃ (X = Cl, Br), and fragmentation of the valence electronic states of PX₃⁺ studied by TPEPICO spectroscopy. *J. Chem. Soc., Faraday Trans.* **1998**, *94* (8), 1045–1050.
(16) Jarvis, G. K.; Boyle, K. J.; Mayhew, C. A.; Tuckett, R. P. Threshold photoelectron—photoion coincidence spectroscopy of perfluorocarbons. 1. Saturated perfluorocarbons C₂F₆, C₃F₈, and n-C₄F₁₀. *J. Phys. Chem. A* **1998**, *102* (19), 3219–3229.
(17) Seccombe, D. P.; Chim, R. Y. L.; Jarvis, G. K.; Tuckett, R. P. The use of threshold photoelectron—photoion coincidence spectroscopy to probe the spectroscopic and dynamic properties of the valence states of CCl₃F⁺, CCl₃H⁺, and CCl₃Br. *Phys. Chem. Chem. Phys.* **2000**, *2* (4), 769–780.
(18) Weitzel, K. M.; Mahnert, J. The binding energies of small Ar, CO, and N₂ cluster ions. *Int. J. Mass Spectrom.* **2002**, *214* (2), 175–212.
(19) Ng, C. Y. Vacuum ultraviolet spectroscopy and chemistry by photoionization and photoelectron methods. *Annu. Rev. Phys. Chem.* **2002**, *53*, 101–140.
(20) Lago, A. F.; Kercher, J. P.; Bodi, A.; Sztaray, B.; Miller, B.; Wurzelmann, D.; Baer, T. Dissociative photoionization and thermochemistry of dihalomethane compounds studied by threshold photoelectron photoion coincidence spectroscopy. *J. Phys. Chem. A* **2005**, *109* (9), 1802–1809.
(21) Franklin, J. L.; Hierl, P. M.; Whan, D. A. Measurement of the translational energy of ions with a time-of-flight mass spectrometer. *J. Chem. Phys.* **1967**, *47* (9), 3148–3153.
(22) Xu, H. F.; Guo, Y.; Li, Q. F.; Shi, Y.; Liu, S. L.; Ma, X. X. Channel switching effect in photodissociating N₂O⁺ ion at 312.5 nm. *J. Chem. Phys.* **2004**, *121* (7), 3069–3073.
(23) Shi, Y.; Li, Q. F.; Wang, H.; Dai, J. H.; Liu, S. L.; Ma, X. X. An approach to obtain the photofragment translational energy distribution from time-of-flight profile. *Acta Phys. Sin.* **2005**, *54* (5), 2418–2423.

(24) Howle, C. R.; Collins, D. J.; Tuckett, R. P.; Malins, A. E. R. Threshold photoelectron–photoion coincidence spectroscopy study of $CHCl_2F^+$, $CHClF_2^+$ and CH_2ClF^+: Steric influence of the chlorine, uorine and hydrogen atoms. *Phys. Chem. Chem. Phys.* **2005**, 7 (11), 2287–2297.

(25) Eppink, A.; Parker, D. H. Velocity map imaging of ions and electrons using electrostatic lenses: Application in photoelectron and photofragment ion imaging of molecular oxygen. *Rev. Sci. Instrum.* **1997**, 68 (9), 3477–3484.

(26) Beebe, N. H. F.; Thulstrup, E. W.; Andersen, A. Configuration interaction calculation of low-lying electronic states of O_2, O_2^+, and O_2^{2+}. *J. Chem. Phys.* **1976**, 64 (5), 2080–2093.

(27) Honjou, N.; Tanaka, K.; Ohno, K.; Taketa, H. Configuration interaction calculation of the O_2^+ ion and study of the photoelectron spectra of O_2. *Mol. Phys.* **1978**, 35 (6), 1569–1578.

(28) Edqvist, O.; Lindholm, E.; Selin, L. E.; Asbrink, L. On the photoelectron spectrum of O_2. *Phys. Scr.* **1970**, 1 (1), 25–30.

(29) Merkt, F.; Guyon, P. M.; Hepburn, J. High-resolution threshold photoelectron spectrum of molecular oxygen. *Chem. Phys.* **1993**, 173 (3), 479–489.

(30) Merkt, F.; Guyon, P. M. Threshold photoelectron spectrum of molecular oxygen in the region of the $B^2\Sigma_g^- \leftarrow X^3\Sigma_g^-$ transition. *J. Phys. Chem.* **1995**, 99 (43), 15775–15778.

(31) Tanaka, T.; Yoshii, H.; Morioka, Y.; Hayaishi, T.; Ito, K.; Hall, R. I. High-resolution threshold photoelectron spectra of molecular oxygen in the 18–24 eV region. *J. Chem. Phys.* **1998**, 108 (15), 6240–6248.

(32) Blyth, R. G. C.; Powis, I.; Danby, C. J. Competing predissociation of $O_2^+(B^2\Sigma_g^-)$. *Chem. Phys. Lett.* **1981**, 84 (2), 272–275.

(33) Bombach, R.; Schmelzer, A.; Stadelmann, J. P. Predissociation of the molecular oxygen cations $^{16}O_2^+$ and $^{18}O_2^+$ studied by photoelectron photoion coincidence spectroscopy. *Int. J. Mass Spectrom. Ion Processes* **1982**, 43 (2–3), 211–225.

(34) Richard-Viard, M.; Dutuit, O.; Lavollee, M.; Govers, T.; Guyon, P. M.; Durup, J. O_2^+ ions dissociation studied by threshold photoelectron photoion coincidence method. *J. Chem. Phys.* **1985**, 82 (9), 4054–4063.

(35) Akahori, T.; Morioka, Y.; Watanabe, M.; Hayaishi, T.; Ito, K.; Nakamura, M. Dissociation processes of O_2 in the VUV region 500–700 A. *J. Phys. B: At., Mol. Opt. Phys.* **1985**, 18 (11), 2219–2229.

(36) Ellis, K.; Hall, R. I.; Avaldi, L.; Dawber, G.; McConkey, A.; Andric, L.; King, G. C. High-resolution threshold photoelectron and photoion spectroscopy of oxygen in the 12–50 eV photon range. *J. Phys. B: At., Mol. Opt. Phys.* **1994**, 27 (15), 3415–3426.

(37) Evans, M.; Stimson, S.; Ng, C. Y.; Hsu, C. W.; Jarvis, G. K. Rotationally resolved pulsed field ionization photoelectron study of $O_2^+(B^2\Sigma_g^-, ^2\Sigma_u^-; v^+ = 0–7)$ at 20.2 - 21.3 eV. *J. Chem. Phys.* **1999**, 110 (1), 315–327.

(38) Lafosse, A.; Brenot, J. C.; Golovin, A. V.; Guyon, P. M.; Hoejrup, K.; Houver, J. C.; Lebech, M.; Dowek, D. Vector correlations in dissociative photoionization of O_2 in the 20–28 eV range. I. Electron-ion kinetic energy correlations. *J. Chem. Phys.* **2001**, 114 (15), 6605–6617.

(39) Wang, S. S.; Kong, R. H.; Shan, X. B.; Zhang, Y. W.; Sheng, L. S.; Wang, Z. Y.; Hao, L. Q.; Zhou, S. K. Performance of the atomic and molecular physics beamline at the National Synchrotron Radiation Laboratory. *J. Synchrotron Rad.* **2006**, 13 (6), 415–420.

(40) Offerhaus, H. L.; Nicole, C.; Lepine, F.; Bordas, C.; Rosca-Pruna, F.; Vrakking, M. J. J. A magnifying lens for velocity map imaging of electrons and ions. *Rev. Sci. Instrum.* **2001**, 72 (8), 3245–3248.

(41) Bodi, A.; Sztaray, B.; Baer, T.; Johnson, M.; Gerber, T. Data acquisition schemes for continuous two-particle time-of-flight coincidence experiments. *Rev. Sci. Instrum.* **2007**, 78, 084102.

(42) Townsend, D.; Minitti, M. P.; Suits, A. G. Direct current slice imaging. *Rev. Sci. Instrum.* **2003**, 74 (4), 2530–2539.

(43) Irimia, D.; Kortekaas, R.; Janssen, M. H. M. In situ characterization of a cold and short pulsed molecular beam by femtosecond ion imaging. *Phys. Chem. Chem. Phys.* **2009**, 11 (20), 3958–3966.

(44) Horio, T.; Suzuki, T. Multihit two-dimensional charged-particle imaging system with real-time image processing at 1000 frames/s. *Rev. Sci. Instrum.* **2009**, 80 (1), 013706.

(45) Tang, X. F.; Niu, M. L.; Zhou, X. G.; Liu, S. L.; Liu, F. Y.; Shan, X. B.; Sheng, L. S. NO^+ formation pathways in dissociation of N_2O^+ ions at the $C^2\Sigma^+$ state revealed from threshold photoelectron–photoion coincidence velocity imaging. *J. Chem. Phys.* **2011**, 134 (5), 054312.

(46) Lu, Y.; He, Z. X.; Cutler, J. N.; Southworth, S. H.; Stolte, W. C.; Samson, J. A. R. Dissociative photoionization study of O_2. *J. Electron Spectrosc. Relat. Phenom.* **1998**, 94 (1–2), 135–147.

(47) Marian, C. M.; Marian, R.; Peyerimhoff, S. D.; Hess, B. A.; Buenker, R. J.; Seger, G. Ab initio CI calculation of O_2^+ predissociation phenomena induced by a spin orbit coupling mechanism. *Mol. Phys.* **1982**, 46 (4), 779–810.

(48) Zare, R. N. Photoejection dynamics. *Mol. Photochem.* **1972**, 4, 1.

(49) Eland, J. H. D.; Duerr, E. J. Anisotropic photoionisation and dissociation through inner valence states of the O_2^+ and NO^+ ions. *Chem. Phys.* **1998**, 229, 1.

6346

dx.doi.org/10.1021/jp111590s |*J. Phys. Chem. A* 2011, 115, 6339–6346